Please cite this article as, "T. Tafsirojjaman, S. Fawzia, D. Thambiratnam, X. Zhao, Study on the cyclic bending behaviour of CFRP strengthened full-scale CHS, Structures. 28 (2020), pp. 741-756 (doi.org/10.1016/j.istruc.2020.09.015)."

Study on the cyclic bending behaviour of CFRP strengthened full-scale CHS members

T. Tafsirojjaman[a,*], Sabrina Fawzia[a], David Thambiratnam[a], Xiao-Ling Zhao[b]

[a] School of Civil Engineering and Built Environment, Faculty of Science and Engineering, Queensland University of Technology, 2 George Street, Brisbane, QLD 4000, Australia.

[b] Department of Civil and Environmental Engineering, The University of New South Wales (UNSW), Sydney, NSW 2052, Australia.

(*Corresponding author: tafsirojjaman@hdr.qut.edu.au,

Email addresses: tafsirojjaman@hdr.qut.edu.au (T. Tafsirojjaman), sabrina.fawzia@qut.edu.au (Sabrina Fawzia), d.thambiratnam@qut.edu.au (David Thambiratnam), xiaolin.zhao@unsw.edu.au (Xiao-Ling Zhao)

Abstract

Circular hollow steel (CHS) members have been regarded as structural elements of choice for use in civil infrastructure. Despite the risk of seismic damage of steel structures during an earthquake due to its cyclic characteristics, studies on the cyclic strengthening of CHSs have been minimal. In the present study, a new finite element (FE) modelling approach is developed and applied to study the cyclic performance of carbon fibre reinforced polymer (CFRP) strengthened CHS specimens. The modelling techniques are first validated using results from the authors' previous experimental work. A detailed parametric study is then carried out to evaluate the effects of CFRP bond length, CFRP layer numbers, ratio of thickness of CFRP to thickness of CHS, CHS member diameter-to-thickness ratio and steel grade on the cyclic performance of the CFRP strengthened CHS members. Results confirm the significant effects of these parameters on the cyclic performance of CFRP strengthened CHS members. The efficiency of CFRP strengthening increases with an increase in the ratio of the thickness of CFRP to the thickness of CHS and also with an increase in the diameter-to-thickness ratio of

CHS specimens. Conversely, the efficiency of CFRP strengthening reduces with an increase in the steel grade. Moreover, the ultimate moment capacities obtained from the FE analyses of the bare and CFRP strengthened CHS specimens agree reasonably well with the theoretically predicted values.

Keywords: Circular hollow section (CHS); CFRP; Strengthening; FE modelling; Cyclic loading; parametric study; Cyclic design factor.

1. Introduction

The use of steel members is continually growing in popularity for structural applications in civil engineering infrastructure. Tubular hollow members are most commonly utilised as they exhibit better bending, compression, torsion, fire resistance and corrosion resistance compared to other open members [1]. However, the seismic response of such members, along with necessary strengthening techniques, are important considerations for their use in seismic regions. The cyclic loading from an earthquake can have devastating effects on structures and cause loss of lives. On average, 2052 deaths per earthquake were recorded between the periods of 1990 to 2010. This adds up to 1.87 million deaths as a result of earthquakes in the 20th century [2]. Construction of steel frames and trusses have utilised tubular hollow members as major structural components in earthquake-prone areas. Tubular hollow members have also been used in buildings and halls as girders, beams, columns and roof space frames. As of recent times, facades have also incorporated tubular hollow members into their design for architectural and structural purposes [1]. Structural defects and failures in buildings resulting from cyclic loads have become a growing concern as earthquakes are capable of causing widespread damage to both on- and offshore structures [3,4]. Offshore structures are affected by additional cyclic loads generated from waves, wind and currents [4]. These offshore structures include jacket type steel structures that are used as supports in gas and oil extraction infrastructure platforms. Jacket-type steel construction involves a space frame that is made by

welding together tubular members. In addition to the adverse effects of cyclic loading, it has been observed that many civil engineering infrastructures can have some structural deficiencies related to errors in design, material property degradation and service load increments. Strengthening and rehabilitation of steel sections is a promising method to mitigate these structural deficiencies. However, studies relating to strengthening and rehabilitation of tubular steel members under cyclic loading have been minimal.

Strengthening and rehabilitation of steel structures are conventionally done by welding of additional steel plates. But the heat produced during welding of the additional steel plates can affect the steel structure by introducing fatigue failure as it can have adverse effects on the stress distribution. The added weight of the newly attached steel plates and corrosion that can lead to long term structural effects are also concerns of this method. Welding of additional steel plates involves large equipment and supports and can cause interruptions to services over long periods [4]. Comparatively, CFRP strengthening techniques do not have these adverse effects when implemented for rehabilitation and strengthening of steel structures. Researchers concluded the CFRP strengthening technique to be a promising method for rehabilitation and strengthening of civil infrastructure [5–8]. CFRP applications have substantial benefits, including high strength-weight ratio, high tensile strength [9,10] and high resistance to corrosion [11,12]. Additionally, CFRP strengthening techniques, reducing the application time and labour, are easily applicable and have high flexibility as they can treat any shape/form. All of these benefits contribute to the cost-efficiency of the CFRP strengthening technique [13,14]. Past studies have proven the efficiency of CFRP strengthening to improve ultimate load capacity [15], enhance energy absorption ability [16] and reduce tip displacement [17–20]. Added benefits include increased impact resistance [21], local buckling delays [22,23] and most importantly, resistance against fatigue of steel joints [24–27]. Currently, there are limited

studies that demonstrate the capability of CFRP strengthening to enhance the bending performance of tubular and rectangular hollow steel members [15,28–30].

The only currently available investigation on the cyclic response of the CFRP strengthened circular hollow section (CHS) steel specimens was carried out by the authors experimentally with limited parameters due to the experimental limitations [29]. Numerical simulation techniques for studying the performance of CFRP strengthened CHS steel members under cyclic loading have, however, not yet been developed. The current numerical study is aimed at the development and application of cyclic simulation techniques to treat CFRP strengthened CHS steel sections followed by a comprehensive parametric investigation to complement and supplement the limited experimental information [29] and to fill the research gap in this area. The numerical simulation techniques are developed in ABAQUS CAE [31] FE software and the simulated results are compared with the authors' published experimental test results [29] to validate the FE modelling techniques. Additionally, a comprehensive parametric investigation is conducted to study the effects of important parameters such as CFRP bond length, CFRP layer numbers, the ratio of the thickness of CFRP composites (t_{CFRP}) to the wall thickness of CHS (t_{CHS}), CHS member diameter-to-thickness ratio and steel grade on the cyclic performance of the CFRP strengthened CHS steel specimens. The structural performance parameters are moment capacity, energy dissipation capability and secant stiffness and results from this detailed parametric study will fill the knowledge gap in this area [29]. Moreover, the ultimate moment capacities from the FE model compare reasonably well with the theoretically predicted values. The information from the present study enabled recommendation of an appropriate cyclic design factor that can be used in designs. The developed FE modelling techniques and the analytical procedure will be beneficial and save experimental time and cost to predict the improvement due to CFRP strengthening on different CHS specimens under cyclic loading.

Research findings will be helpful for restoring the structural integrity of CHS members in earthquake-prone areas through CFRP strengthening.

2. Experimental study

The experimental investigation on the cyclic response of the bare and CFRP strengthened CHS steel specimens was carried out by the authors in the previous study [29]. All the CHS steel specimens had identical dimensions with the specimen thickness and the outer diameter of 4 mm and 101.6 mm respectively. One specimen remained bare as a control specimen (BB-C) out of the cyclic tested specimens. The other two specimens were strengthened by CFRP with a bond length of 900 mm from the support end and LHL (with CFRP fibre orientations in the longitudinal, hoop and again longitudinal directions in the first, second and third layers respectively) fibre orientation. Two different types of epoxy adhesives: Mbrace saturant in SB-C-1 specimen and Araldite K630 in the SB-C-2 specimen were used as bonding materials and the effects of the types of adhesive were investigated [29]. The details of the specimens are given in Table 1. The detailed procedure of the CFRP strengthening technique can be found in Tafsirojjaman et al. [29]. The CFRP strengthened CHSs were then cured for at least two weeks under ambient temperature and tested under cyclic loading. The cyclic loading protocol proposed by ANSI/AISC [3], shown in Figure 1(a), was chosen and applied with a quasi-static rate and displacement control at the tip of the specimens while the other support end constrained was fixed. The input displacement was applied through two pinned hinges in order to prevent the application of any axial load and study the pure bending behaviour of the CHS members. More details on experimental testing can be found in Tafsirojjaman et al. [29]. Figure 1(b) has captured the experimental setup schematic diagram.

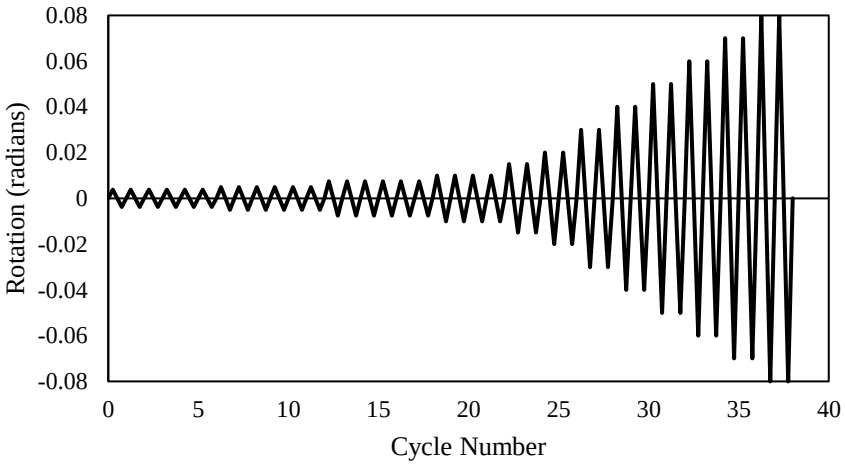

(a)

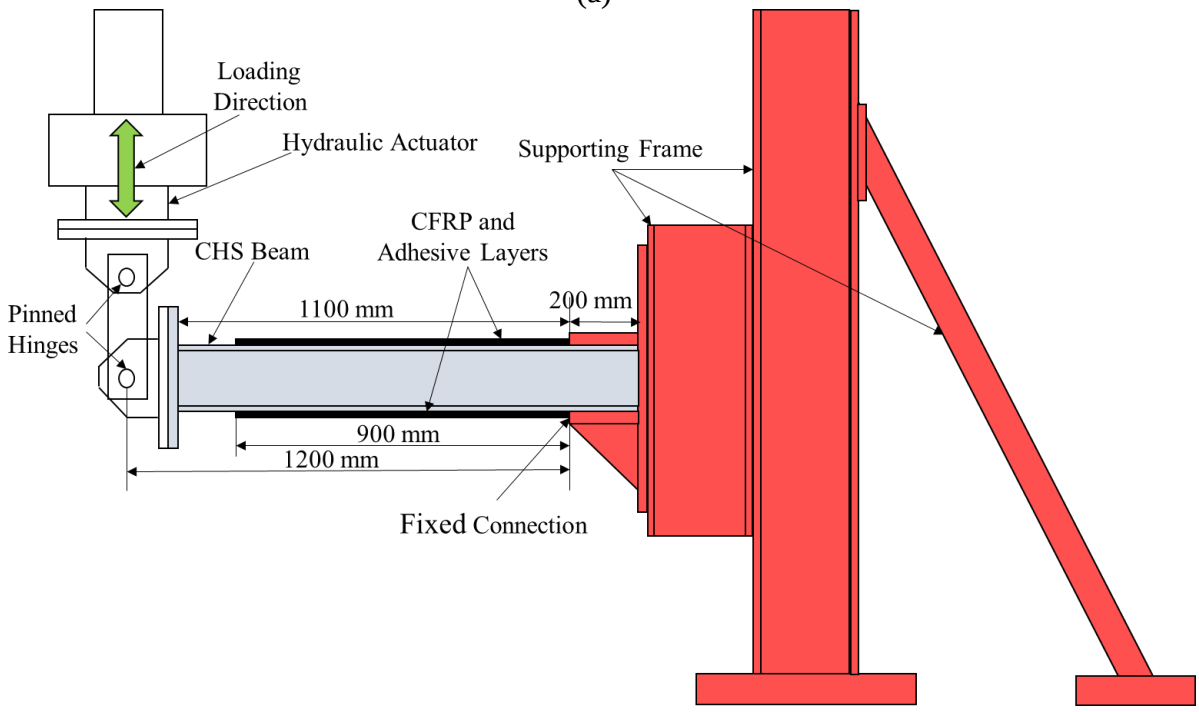

(b)

Figure 1: (a) AISC cyclic loading protocol [3] and (b) Schematic diagram of experimental setup [29].

Table 1:Matrix of experimentally tested specimens.

Specimen notation	Adhesive types	Types of Specimen
BB-C	-	Bare Beam
SB-C-1	Mbrace saturant	Strengthened Beam
SB-C-2	Araldite K630	Strengthened Beam

3. FE modelling and validation

The numerical simulation is conducted with the three-dimensional ABAQUS CAE [31] FE software package. The developed FE model and the cyclic simulation are validated by comparing it with the author's available experimental study [29]. Queensland University of Technology (QUT) has the facility of high-performance computing (HPC), which has been utilised to reduce the simulation time of detailed numerical investigations.

3.1. FE model

The steel sections of the strengthened CHS and bare (control) CHS specimens are identical and modelled with the specimen thickness of 4 mm, the outer diameter of 101.6 mm and a length of 1100 mm (as in the experiments) using the FE software. To simulate the strengthened members, CFRP and adhesive have been modelled for a length of 900 mm. The adopted CFRP layer thickness of 0.60 mm has been taken from the experimental study [29]. The layer of adhesive has an assumed thickness of 0.1 mm, as per previous studies [32]. As the dry CFRP fabrics were applied in adhesive wetted CHS members and the later CFRP layers continued with wet lay-up process during the experimental investigation, only an adhesive layer is modelled between the CFRP composite and steel interface to capture the debonding between the CFRP composite and steel in the model if any.

A central reference node has been created at the centre of the cross-section of each end of CHS and the CHS member’s peripheral nodes are constrained to the reference node via Multiple Point Constraint (MPC) type beams. To accurately represent the experimental setup, the specimens tip reference node has been modelled at the loading point and made free for all degrees of freedom (rotational and translational) while the supported end reference node was made fixed in all degrees of freedom.

The steel section was modelled with reduced integration and hourglass control of the 4-node shell element (S4R). In the model, 8-node three-dimensional cohesive elements (COH3D8) are

used for the adhesive layer, since this type of element can predict the cohesive behaviour and failure [33–36]. The CFRP layers are modelled by continuum shell elements of the 8-node quadrilateral with reduced integration and hourglass control (SC8R). Continuum shell elements can predict the failure of composites accurately and are most suitable for the modelling of CFRP composites [33–38]. The modelling of both continuum shell and cohesive elements has been done by assigning solid offsetting in the outward direction of orphan mesh. Each of the longitudinal and transverse layers of CFRP is created with different parts to attribute the CFRP fibre orientation. The connection between the adhesive and CFRP composite interacting surfaces is established by shearing the notes. In addition, tie constraint is used for bonding between the steel surface and the CFRP composites. To ensure efficiency and accuracy within the model, the optimisation of mesh size is confirmed through a mesh-convergence study. The details of the FE model of CFRP strengthened CHS member are shown in Figure 2.

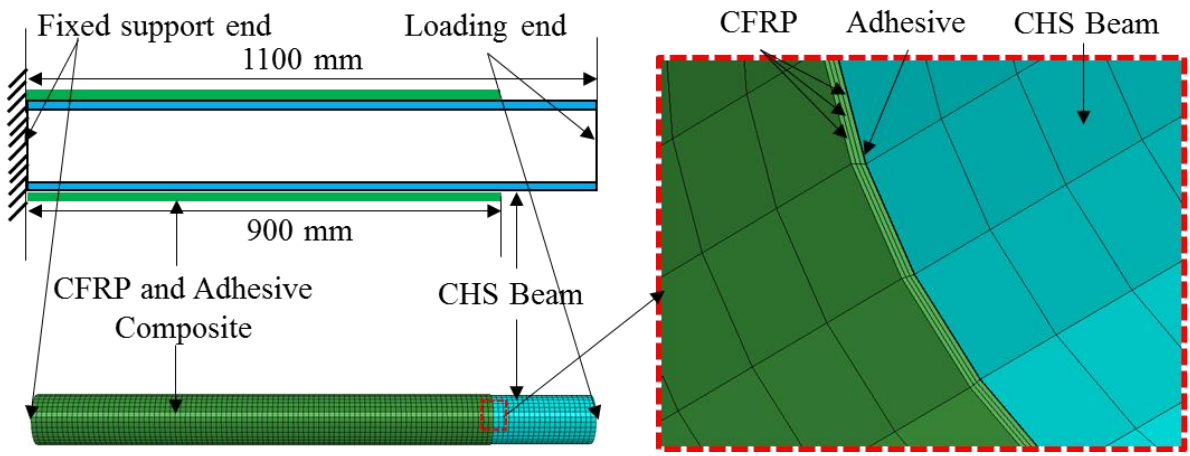

Figure 2: Details of the FE model.

3.2. Material model and properties

3.2.1. Steel

To more accurately capture the inelastic hysteretic behaviour and strain hardening, the combined isotopic-kinematic hardening law with no strain rate effects has been employed. For all FE models, the steel properties are taken from the experimental investigation [29] where

the values of elastic modulus, tensile strength and yield strength are 190 GPa, 367 MPa and 320 respectively. The value of the steel poison ratio in the model is used as 0.3 [32].

3.2.2. Adhesive

The traction between the steel outer surface and the CFRP has been simulated by applying an adhesive layer. The adhesive layer is created in the FE model by using coupled cohesive zone modelling, which is based on traction separation law. This law accounts for the separations and attractions in a three-dimensional plane: normal direction and two shear directions parallel to the interface. The normal and shear separations are represented with δ_n, δ_s and δ_t whereas the corresponding tractions are represented with t_n, t_s and t_t respectively.

It is assumed that there is a linear response for the adhesive (cohesive elements) until the initiation of damage [23,24]. Then the behaviour of damage initiation on the interface can be represented by,

$$\begin{bmatrix} t_n \\ t_s \\ t_t \end{bmatrix} = \begin{bmatrix} k_{nn} & 0 & 0 \\ 0 & k_{ss} & 0 \\ 0 & 0 & k_{tt} \end{bmatrix} \begin{bmatrix} \delta_n \\ \delta_s \\ \delta_t \end{bmatrix} \qquad \text{Equation 1}$$

In the above equation, the elastic stiffnesses in the normal and shear directions are represented by $k_{nn,}\, k_{ss}$ and k_{tt} respectively and the normal direction is governed by the mode-I failure, whereas the shear directions governed by the mode-II failure. k_{nn} is given by the bond separations initial slope model shape for mode-I loading.

$$k_{nn} = \frac{E_a}{T_o} \qquad \text{Equation 2}$$

where the thickness of the adhesive and the elastic modulus are denoted by T_o and E_a respectively. The value of E_a is obtained from experimental research [29] and listed in Table

2. k_{ss} and k_{tt} are assumed equal according to Teng et al. (2015) and determined from the mode-II loading initial slope and represented as [36],

$$k_{ss} = k_{tt} = 3\left(\frac{G_a}{T_0}\right)^{0.65} \quad \text{Equation 3}$$

where the modulus of shear for the adhesive is represented by G_a. The adhesive stiffness values should produce adequate stiffness without being too stiff to cause oscillation in the interface [15]. The values of k_{nn}, k_{ss} and k_{tt} cannot be obtained directly from the experiment; however, a reasonable approximate initial value of k_{nn}, k_{ss} and k_{tt} can be possible from Equation 2 and Equation 3. Then the reasonable value of k_{nn}, k_{ss} and k_{tt} can be confirmed by comparing with the experimental results [39]. The given values of k_{nn}, k_{ss} and k_{tt} in Table 2 are taken from the author's available research [15] where the used adhesive was the same.

Mixed-mode failure criteria (QUADS) defined the damage initiation during the current investigation and it considered both mode-I and mode-II loading effects (Equation 4) [31]; when the value of one is reached in the function, it can be assumed that damage has occurred. As the compressive stress loads do not provide damage to the element t_n, t_s and t_t have a value of zero under compression as donated by the symbol '⟨⟩'.

$$\left\{\frac{\langle t_n \rangle}{\sigma_{\max}}\right\}^2 + \left\{\frac{\langle t_s \rangle}{\tau_{\max}}\right\}^2 + \left\{\frac{\langle t_t \rangle}{\tau_{\max}}\right\}^2 = 1 \quad \text{Equation 4}$$

where $\tau_{\max}$ is the maximum stress in the tearing and sliding direction of the contact while the maximum stress in the opening direction is represented by $\sigma_{\max}$. The values of $\sigma_{\max}$ for both types of adhesive are obtained from experimental research [29] and listed in Table 2. Moreover, $\sigma_{\max}$ and $\tau_{\max}$ are assumed as equal [15].

After meeting the damage initiation criteria, the stiffness of the adhesive material starts to degrade and a phenomenon called damage evolution begins. A linear softening approach based on energy was used to emulate the damage evolution in ABAQUS using the mixed model law based on Benzeggah-Kenane (BK) fracture energy equation (Equation 5) [40].

$$G_I + (G_{II} - G_I)\left(\frac{G_s}{G_t}\right)^{\eta} = G_n \qquad \text{Equation 5}$$

where work is done in the normal and shear directions are G_n, G_s and G_t, while G_I and G_{II} correspond to the maximum fracture energies that cause failure in normal and shear directions respectively. Alam et al. [33] provided the G_I and G_{II} values. The material properties as shown in Table 2, for the adhesive used in the ABAQUS model.

Table 2: Properties of adhesive.

Property	Mbrace Saturant	Araldite K630
E_a	2.86 GPa	6.5 GPa
$\sigma_{\max}$	46 MPa	33 MPa
k_{nn}	2.8×10^{13} N/m^3	6.07×10^{13} N/m^3
$k_{ss}=k_{tt}$	1.4×10^{13} N/m^3	3.03×10^{13} N/m^3
G_I	1000 N/m	1000 N/m
G_{II}	1250 N/m	1250 N/m

3.2.3. CFRP

The CFRP composite has been modelled by using the elastic-lamina type material model and the damage applied to it is emulated by using the Hashin failure criteria model [41,42]. The CFRP displayed the behaviour of damage without showing any significant deformation. The Hashin model can effectively predict the material damage of the CFRP [43]. Four distinctive modes of failure are considered in the model for the CFRP: (a) Fibre rupture under tension (F_f^t); (b) Fibre buckling under compression (F_f^c); (c) Transverse tension and shear causing

matrix cracking (F_m^t); (d) Crushing of the matrix under transverse compression and shear (F_m^c). The criteria to initiate damage must occur for one of the failure modes when a value of one or higher is achieved. To determine the criteria above, the following equations are used.

$$F_f^t = \left(\frac{\sigma_{11}}{T^L}\right)^2 + \alpha\left(\frac{\sigma_{12}}{S^L}\right)^2$$

$$F_f^c = \left(\frac{\sigma_{11}}{C^L}\right)^2$$

$$F_m^t = \left(\frac{\sigma_{22}}{T^T}\right)^2 + \left(\frac{\sigma_{12}}{S^L}\right)^2$$

$$F_m^c = \left(\frac{\sigma_{22}}{2S^T}\right)^2 + \left[\left(\frac{\sigma_{12}}{2S^T}\right)^2 - 1\right]\frac{\sigma_{22}}{C^T} + \left(\frac{\sigma_{12}}{S^L}\right)^2 \qquad \text{Equation 6}$$

Transverse and longitudinal directions are indicated by the subscripts of T and L, while the shear, tensile and compressive strengths are represented by S, T and C respectively. Components of the stress tensor are indicated by σ_{11}, σ_{22} and σ_{12}. When the criteria for damage evolution is achieved, it initiates the damage of the failure mode. It is successful when the criteria for fracture energy is exceeded by the energy being dissipated within the model. Hence, for the FE model to work, the energy required for each failure mode needs to be accounted for. The average modulus of elasticity (E_{IC}) and tensile strength (T^L) obtained from the experimental research [15,29] are displayed in Table 3. Furthermore, the facture energies are provided in Table 3 for each failure criteria, obtained from Faggiani and Falzon [38]. Fracture energy is represented by *G*, and compression, tension, matrix and fibre is represented by the subscripts *c, t, m,* and *f* respectively. The compressive strength (C^L) for CFRP is supposed as 20% of its tensile strength [44]. The tensile/compressive strengths in the transverse direction and the shear strengths in the longitudinal/transverse direction are taken as 10 percent of the

tensile strength [44] which is within the assumed range [38,43]. The CFRP poisson's ratio is taken as 0.33 [32].

Table 3: CFRP composite properties.

Property	Value
E_{1C}	75 GPa
E_{2C}	25 MPa
T^{L}	987 MPa
G_{ft}	91,600 N/m
G_{fc}	79,900 N/m
G_{mc}	1100 N/m
G_{mt}	220 N/m

3.3. Validation

The FE model simulated results are compared with the results of the experimental study to validate the FE modelling techniques. The comparisons of the FE model simulated hysteresis behaviours with the experimental hysteresis behaviours of the bare and CFRP strengthened CHS specimens have been presented in Figure 3. A good matching can be found between the two sets of experimental and FE model simulated hysteresis behaviours and the mean ratio and COV of ultimate moment capacities are 0.98 and 0.016 respectively. In addition, the comparisons of the FE model simulated and the experimental secant stiffness of the bare and CFRP strengthened steel specimens are depicted in Figure 4. To calculate the secant stiffness of a particular rotational level, the load at the maximum displacement of that particular rotational level is divided by the maximum displacement of that rotational level. A good agreement is observed between the FE model simulated and experimental secant stiffnesses of the bare and CFRP strengthened steel specimens, and the mean ratio and COV of stiffnesses are 0.97 and 0.029 respectively. Moreover, the experimental and FE model simulated energy

dissipation capacities at the maximum rotational level of the bare and CFRP strengthened specimens are compared. Experimental and FE model simulated ultimate moment capacities, secant stiffnesses (at ultimate moment capacity point of 0.04 rad. of the bare specimen) and energy dissipation capacities are compared as shown in Table 4. The three sets of results compare reasonably well, however, with small variations due to the (observed) uncertain flexibility of sandwiched rigid support connection during cyclic testing [29]. The accuracy and validation of the FE modelling techniques can, therefore, be confirmed from the above discussion.

Table 4: Comparison between experimental and FE simulated results.

Structural parameters	Specimen notation	Experimental results	FE results	$\frac{FE\ results}{Experimental\ results}$
Moment capacity (kN.m)	BB-C	12.90	12.94	1.00
	SB-C-1	17.10	16.70	0.98
	SB-C-2	17.34	16.76	0.97
			Mean ratio	0.98
			COV	0.016
Secant stiffness (kN/m)	BB-C	206.71	208.69	1.01
	SB-C-1	290.25	276.59	0.95
	SB-C-2	288.21	273.12	0.95
			Mean ratio	0.97
			COV	0.029
Energy dissipation capacity (kN.m)	BB-C	4.11	4.76	1.16
	SB-C-1	4.89	4.90	1.00
	SB-C-2	5.08	4.84	0.95
			Mean ratio	1.04
			COV	0.089

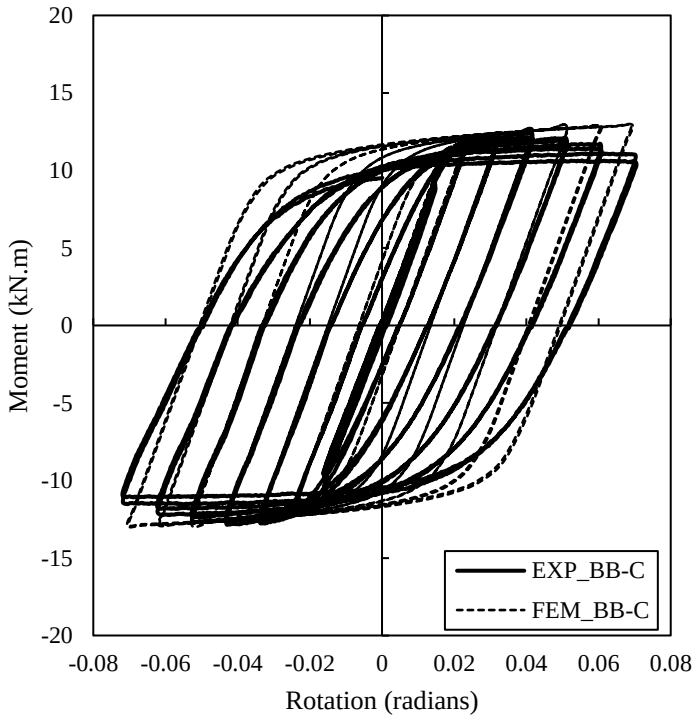
20
15
10
5
0
-5
-10
-15
-20
Moment (kN.m)
-0.08
-0.06
-0.04
-0.02
0
0.02
0.04
0.06
0.08
Rotation (radians)
EXP_BB-C
FEM_BB-C

(a)

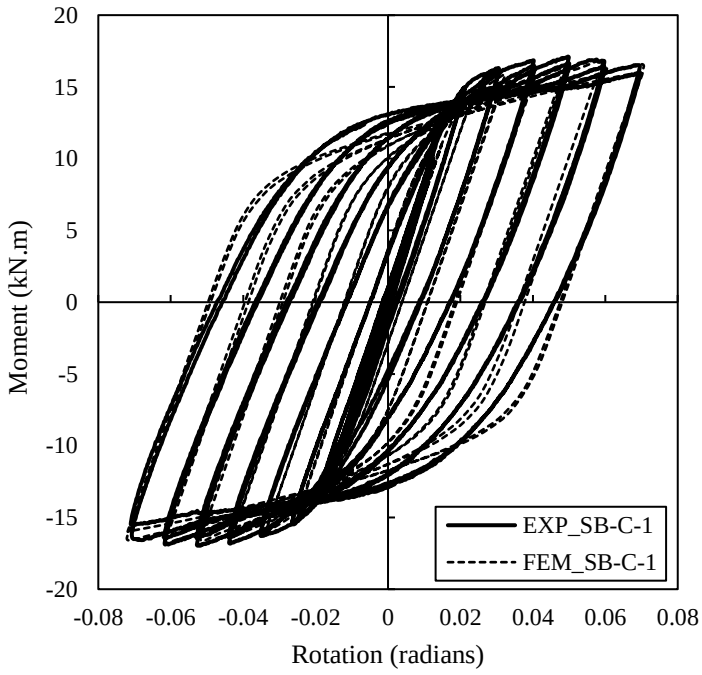
20
15
10
5
0
-5
-10
-15
-20
Moment (kN.m)
-0.08
-0.06
-0.04
-0.02
0
0.02
0.04
0.06
0.08
Rotation (radians)
EXP_SB-C-1
FEM_SB-C-1

(b)

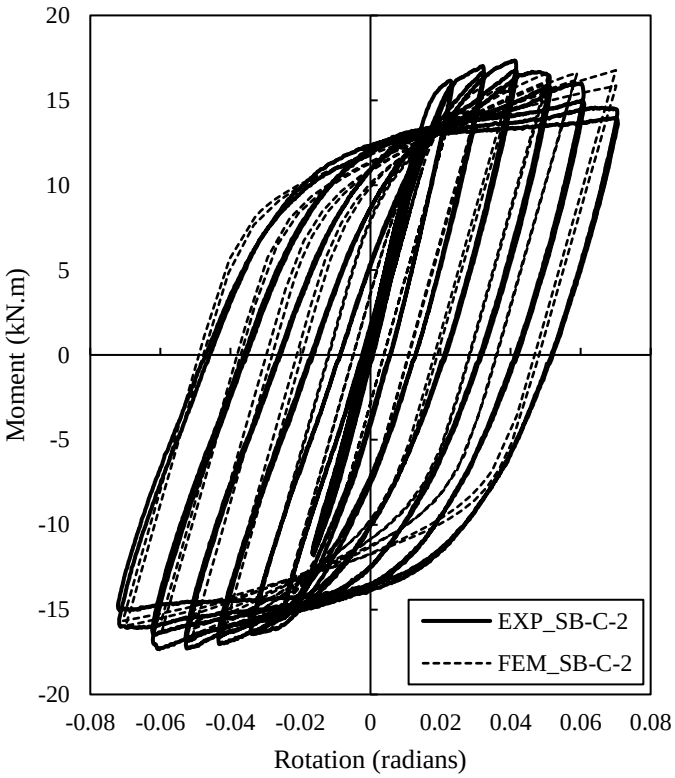

(c)

Figure 3: Comparison of the hysteresis behaviours of the (a) bare CHS specimen (b) CFRP strengthened specimen (SB-C-1) (c) CFRP strengthened specimen (SB-C-2).

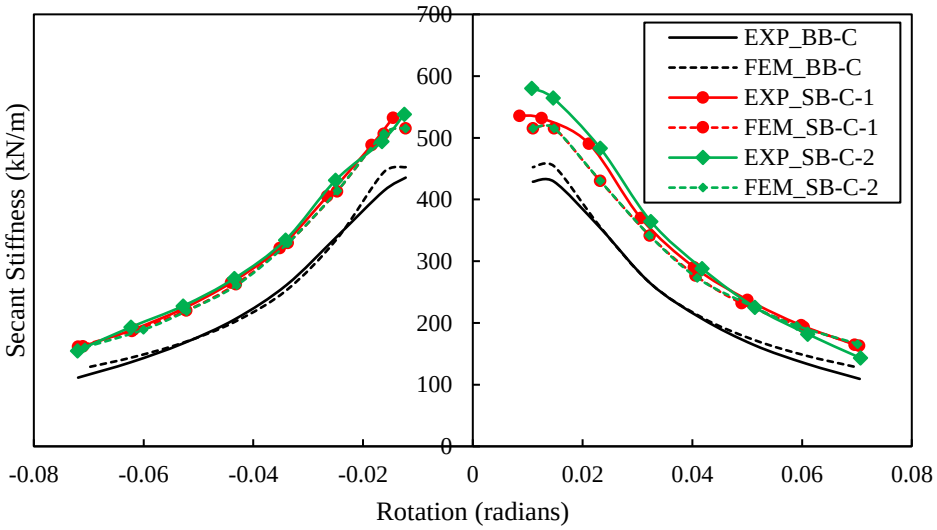

Figure 4: Comparison of the secant stiffness responses of the bare and CFRP strengthened specimens.

4. Parametric Investigation

The comprehensive parametric investigation has been carried out to study the influence of important parameters such as the effects of CFRP bond length, CFRP layer numbers, the ratio of the thickness of CFRP composites (t_{CFRP}) to the wall thickness of CHS (t_{CHS}), CHS members diameter-to-thickness ratio and steel grade on the CFRP strengthened CHS steel specimens cyclic performance, with respect to moment capacity, energy dissipation capability and secant stiffness.

4.1. Effect of CFRPs bond length

The tested specimens were strengthened with CFRPs bond length of 900 mm from the support end, which was almost 82% of the total length of the specimens. Hence investigating the most effective bond length of CFRP composites is very important for minimising the cost of CFRP strengthening projects in civil engineering infrastructures. The CFRP composites wrapping length was varied to find out the most effective bond length for the different structural behaviours of CFRP strengthened CHS steel specimens under cyclic loading. In addition to 900 mm initial strengthening length of CFRP, the CHS steel specimens were strengthened with three other CFRP strengthening lengths of 200 mm, 300 mm and 400 mm. The structural behaviours of these CFRP strengthened CHS specimens in terms of moment capacity backbone response, ultimate moment capacity, stiffness and dissipation of energy, are shown in Figure 5. The moment at the maximum displacement of each rotational level has been plotted against that particular rotational level to create the moment capacity backbone curves. Moreover, for a particular rotational level, the energy dissipation capacity is measured by determining the total bounded area of every cycle at that particular level of rotation. It can be seen from the Figure 5 that the responses of different structural behaviours of strengthened CHS specimens with CFRP under cyclic loading in terms of moment capacity backbone curves, maximum moment capacity, stiffness and dissipation of energy are steadily enhanced with increasing the bond

length up to 300 mm. There is also a small improvement in the cyclic performance of these strengthened CHS specimens up to bond length of 400 mm. But, beyond the bond length of 400 mm the CFRP strengthened CHS steel specimens exhibited either insignificant or no changes in the different structural performances. Strengthened CHS specimens with 100 mm, 200 mm, 300 mm, 400 mm, 600 mm and 900 mm bond lengths of CFRP showed 9.17%, 20.26%, 27.27%, 29.08%, 29.37% and 29.57% improvement of ultimate moment capacity compared to their bare CHS member. These results indicate that the effective bond lengths can be chosen between 300 mm and 400 mm. As there are so many uncertainties when structures are subjected to cyclic loading, the higher bond length of 400 mm is recommended as the effective bond length based on the specific span length and support conditions considered in the present study and used in further parametric investigation, just to be on the safe side.

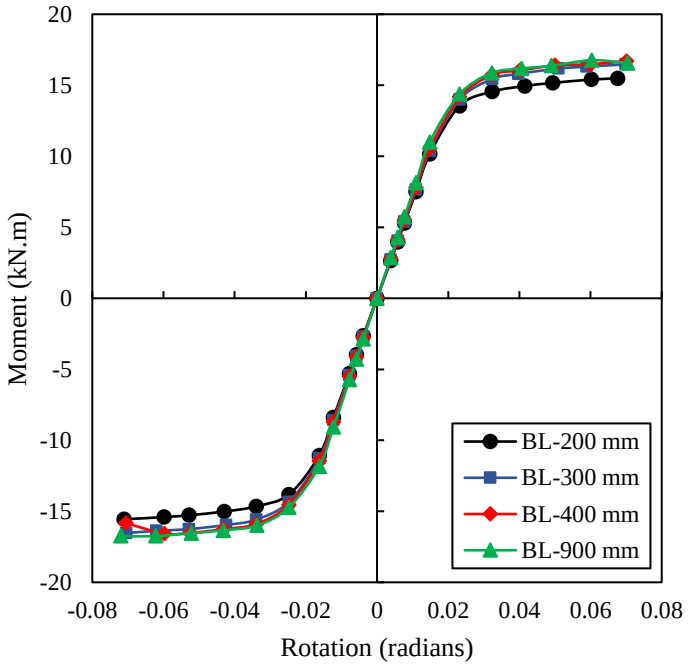

(a)

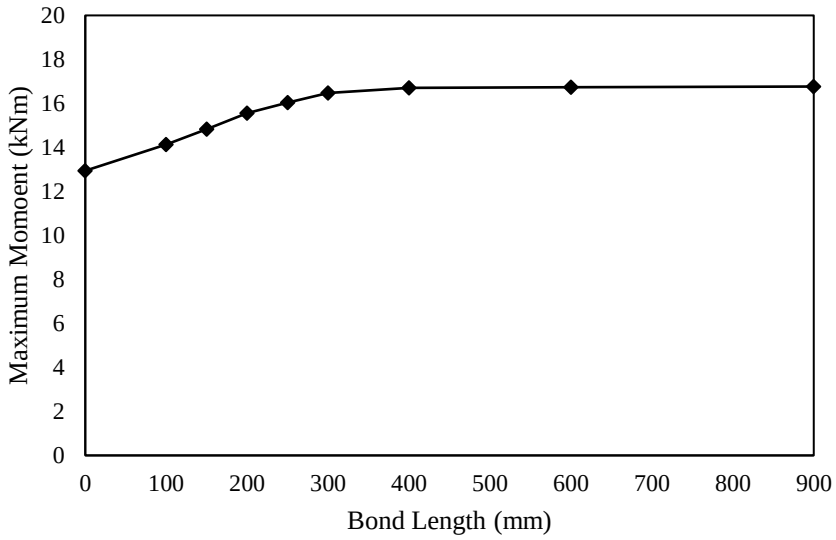
Maximum Momoent (kNm)
20
18
16
14
12
10
8
6
4
2
0
0
100
200
300
400
500
600
700
800
900
Bond Length (mm)

(b)

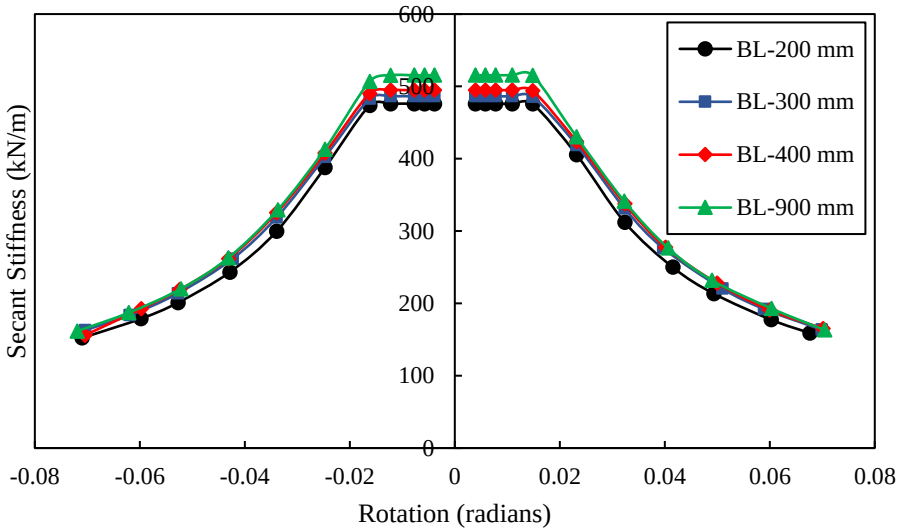
Secant Stiffness (kN/m)
600
500
400
300
200
100
0
-0.08
-0.06
-0.04
-0.02
0
0.02
0.04
0.06
0.08
Rotation (radians)
BL-200 mm
BL-300 mm
BL-400 mm
BL-900 mm

(c)

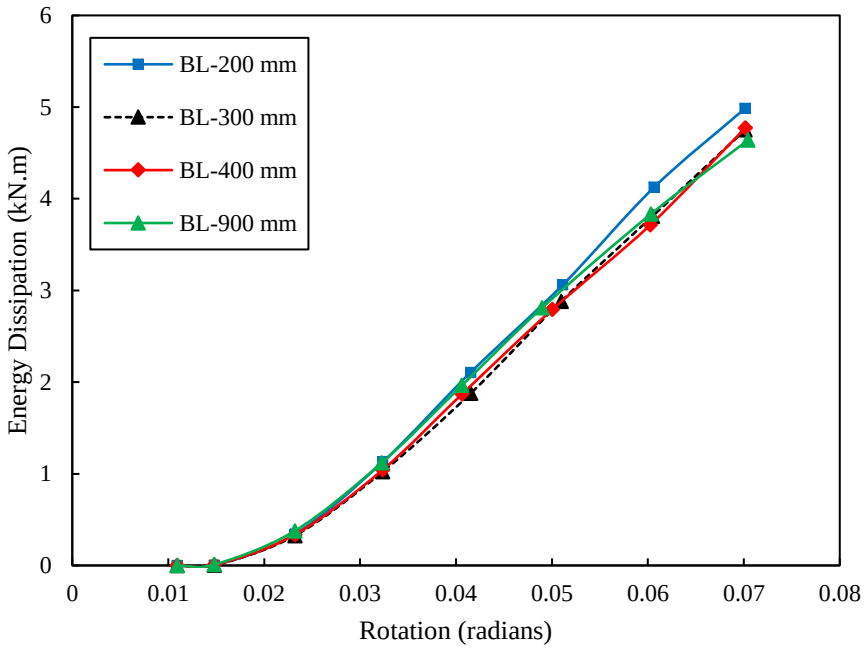

(d)

Figure 5: (a) Moment-rotation backbone responses (b) ultimate moment capacity (c) stiffness and (d) dissipation of energy of strengthened CHS specimens with various bond lengths of CFRP.

4.2. Effect of layers number of CFRP

The CHS steel specimens strengthened with a constant bond length of 400 mm and one to two layers of CFRP composites are considered to find out the most effective number of CFRP layers to strengthen the CHS steel specimens. Results for the response parameters of moment capacity backbone response, ultimate moment capacity, stiffness and dissipation of energy are shown in Figure 6.

It can be seen from these Figures that the cyclic performances of the CFRP strengthened CHS steel members with respect to all the above-mentioned response parameters increase with an increase in the number of CFRP layers. These seem to occur in two stages, an initial increase up to two layers and then a higher increase (in all the response parameters) when the number of composites layers increased from two to three layers. However, the effect of increasing the

layer numbers of CFRP composites beyond three layers has either very little or insignificant effects in these cyclic responses. It can hence be concluded that the responses of the different structural behaviour of CFRP strengthened CHS steel members under cyclic loading is enhanced with increasing the layer numbers of CFRP composite. Moreover, three layers of CFRP composite is the most efficient and cost-effective way to strengthen the CHS steel members. This parametric investigation will be beneficial for minimising the costs of CFRP strengthening of civil engineering infrastructure.

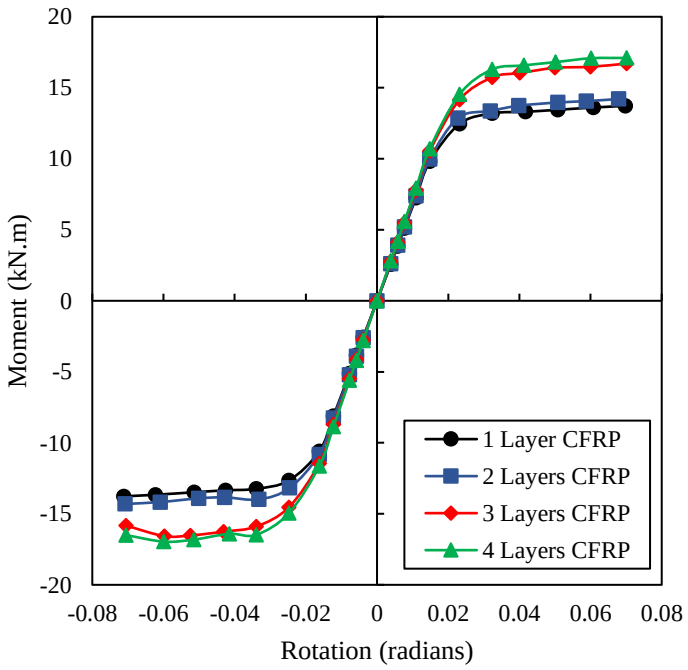

(a)

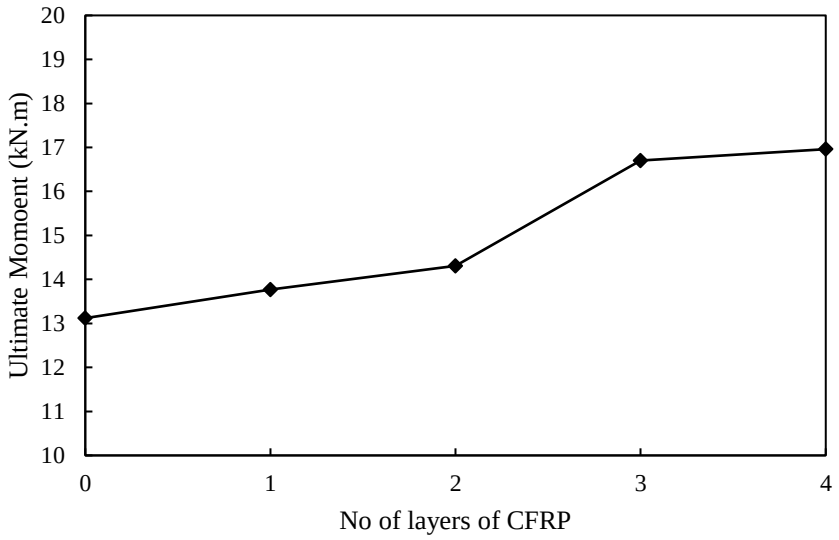
Ultimate Momoent (kN.m)
20
19
18
17
16
15
14
13
12
11
10
0
1
2
3
4
No of layers of CFRP

(b)

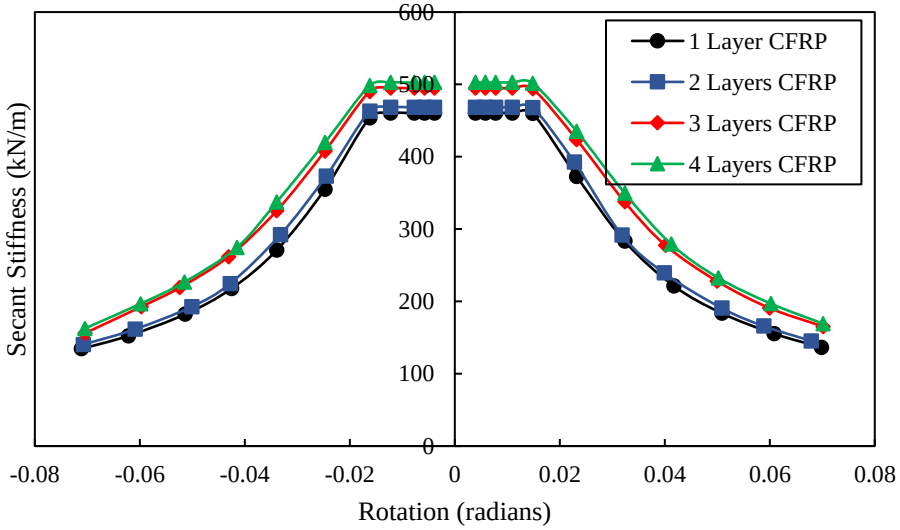
Secant Stiffness (kN/m)
600
500
400
300
200
100
0
-0.08
-0.06
-0.04
-0.02
0
0.02
0.04
0.06
0.08
Rotation (radians)
1 Layer CFRP
2 Layers CFRP
3 Layers CFRP
4 Layers CFRP

(c)

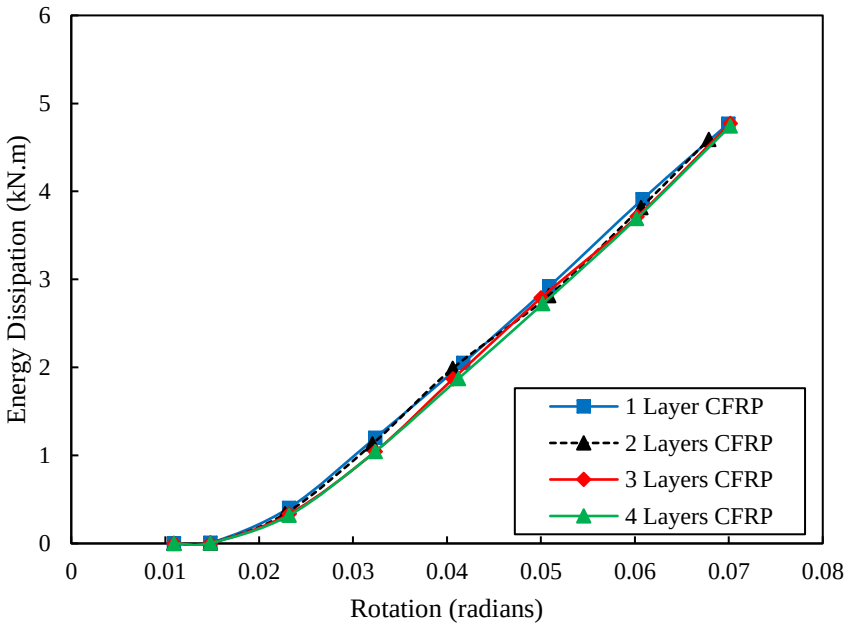

(d)

Figure 6: (a) Moment-rotation backbone responses (b) ultimate moment capacity (c) stiffness and (d) dissipation of energy of strengthened CHS specimens with various layers number of CFRP.

4.3. Effect of the ratio of t_{CFRP}/t_{CHS}

It was shown earlier that use of three layers of CFRP composite is most effective for strengthening CHS steel specimens to enhance their cyclic performance in terms of cyclic hysteresis behaviour, moment capacity backbone curves, secant stiffness and energy dissipation capacity. Hence, CHS steel specimens will be strengthened with only three layers of CFRP and 400 mm bond lengths of CFRP composites in all further investigations on the effects of all other parameters.

Three CHS members with a constant outer diameter (101.6 mm) but with different wall thicknesses of 3.2 mm, 3.6 mm and 4 mm are considered and strengthened with three layers of CFRP and 400 mm bond lengths of CFRP composites to investigate the effect of the ratio of the thickness of CFRP composites to the wall thickness of CHS on the cyclic responses of these

specimens. As the thickness of applied CFRP is constant for all the CHS members, the ratio of t_{CFRP}/t_{CHS} is decreasing with the increasing of CHS wall thickness from 3.2 mm to 3.6 mm to 4 mm. The cyclic hysteresis behaviour of the different sized bare and CFRP strengthened CHS specimens of 101.6×3.2, 101.6×3.6 and 101.6×4.0 are compared in Figure 7 (a), Figure 7 (b) and Figure 7 (c) respectively. In general, both bare and CFRP strengthened CHS specimens showed the full hysteretic loops and confirmed their proper inelastic behaviour capacity. In addition, Figure 8 (a) showed the hysteresis backbone responses of bare and CFRP strengthened CHS specimens with various t_{CFRP}/t_{CHS} ratios. From Figure 7 and Figure 8 (a), it can be noticed that all of the bare and CFRP strengthened CHS specimens ensured the stable responses for both positive and negative rotations by exhibiting an appropriate symmetrical response in both directions. Moreover, all the CFRP strengthened CHS specimens showed a higher moment capacity compared to their bare counterparts and confirmed the efficiency of CFRP strengthening for the CHS specimens under cyclic loading. As a result of CFRP strengthening, the maximum moment capacity of bare CHS 101.6×3.2, 101.6×3.6 and 101.6×4.0 specimens are improved from 10.43 kN.m to 14.27 kN.m, 11.70 kN.m to 15.45 kN.m and 12.94 kN.m to 16.70 kN.m respectively. This equates to the enhancement of maximum moment capacities through CFRP strengthening of CHS specimens with 3.2 mm, 3.6 mm and 4 mm wall thickness by 36.88%, 32.07% and 29.08% respectively.

Figure 8 (b) shows the secant stiffnesses of the bare and CFRP strengthened CHS specimens with various t_{CFRP}/t_{CHS} ratios. The efficiency of CFRP strengthening can be confirmed again as the CFRP strengthened CHS steel specimens have shown an improvement in the secant stiffness in all three cases. The CFRP strengthened CHS 101.6×3.2, 101.6×3.6 and 101.6×4.0 specimens are showed higher maximum secant stiffness of 416.48 kN/m, 455.97 kN/m and 494.75 kN/m respectively, compared to the maximum secant stiffness of 374.49 kN/m, 413.84 kN/m and 453.85 kN/m of their respective bare counterparts. This equates to the enhancement

of secant stiffnesses of 11.21%, 10.18% and 9.01% through CFRP strengthening of bare CHS specimens of 3.2 mm, 3.6 mm and 4 mm wall thickness respectively. In addition, at the end of cyclic loading, the CFRP strengthened CHS steel specimens of 3.2 mm, 3.6 mm and 4 mm wall thicknesses showed 8.28%, 4.82% and 3.04% less stiffness degradation respectively, compared to their bare counterparts, although increased degradation of the secant stiffness with increase in the cyclic rotational level was evident for both bare and CFRP strengthened CHS specimens. Moreover, at the end of the cyclic loading, the secant stiffnesses of CFRP strengthened CHS steel specimens with 3.2 mm, 3.6 mm and 4 mm wall thicknesses are higher than their bare counterparts by 46.88%, 28.83% and 20.66% respectively.

The comparisons of the energy dissipation capacities of the bare and CFRP strengthened CHS steel specimens with different wall thicknesses are depicted in Figure 8 (c). At the early stages of rotations, the bare CHS specimens seem to display higher energy dissipation capacities compared to their retrofitted counterparts. Only at the highest rotation level, the energy dissipation capacities of the retrofitted members show a small enhancement over those of their bare counterparts. At the end of the rotation, the CFRP strengthened CHS 101.6×3.2 showed the highest improvement in the energy dissipation capacity, whereas the CFRP strengthened CHS 101.6×4.0 showed the lowest improvement.

The failure modes of steel section of bare and CFRP strengthened CHS specimens with various t_{CFRP}/t_{CHS} ratios are shown in Figure 9. It is evident that all the CFRP strengthened CHS specimens showed less local buckling compared to the bare CHS specimens as the wrapped CFRP composites contribute to enhance the stiffness and distribute stresses more uniformly. Moreover, the contribution of the CFRP composite for enhancing the stiffness and distributing the stresses more uniformly is more pronounced with the increase in the ratio of t_{CFRP}/t_{CHS}. As a result, the stress distribution at the support end is more evenly distributed and the potential for local buckling is reduced with increased t_{CFRP}/t_{CHS} ratio. Hence, finally, it can be concluded

that the ratio of t_{CFRP}/t_{CHS} has a significant influence on the performance or response parameters of CFRP strengthened CHS steel members under cyclic loading. The efficiency of CFRP strengthening increases when the ratio of the thickness of CFRP composites to the wall thickness of CHS increases.

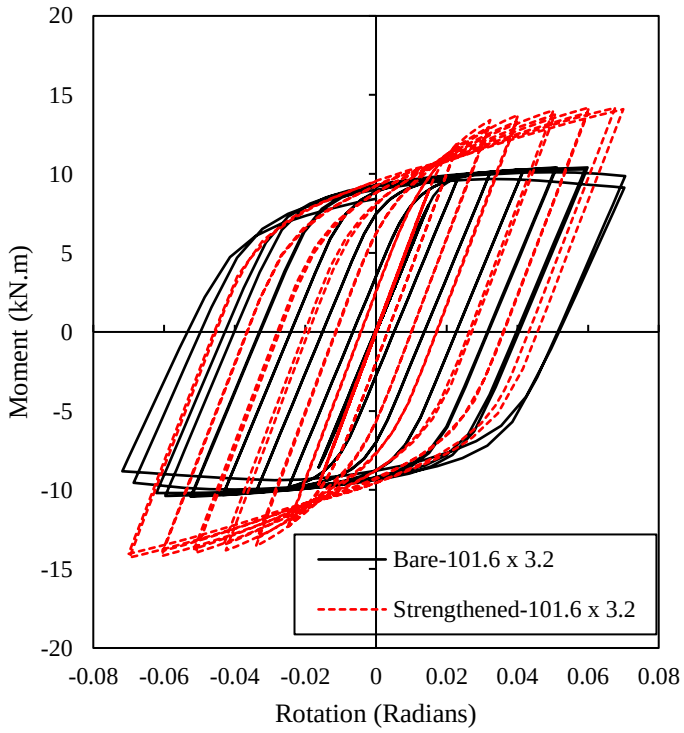

(a)

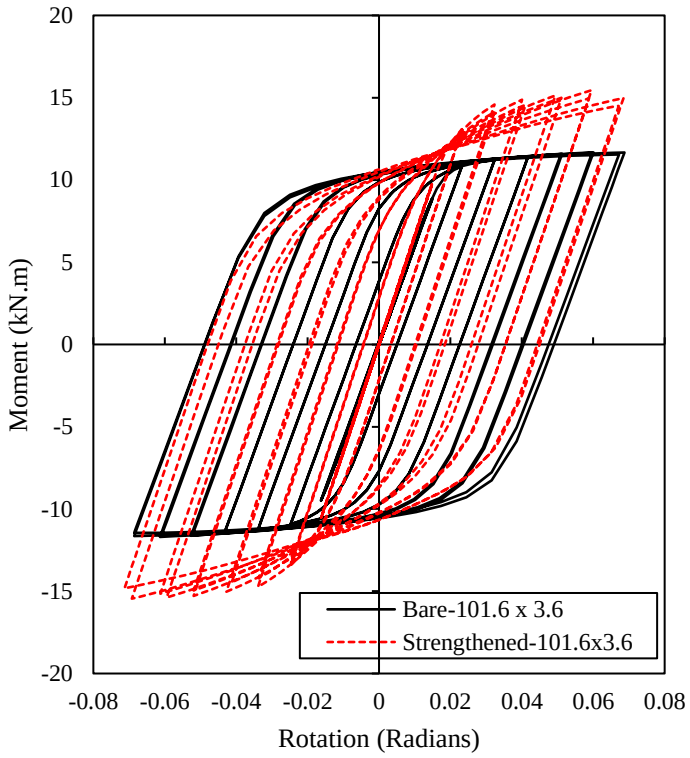

(b)

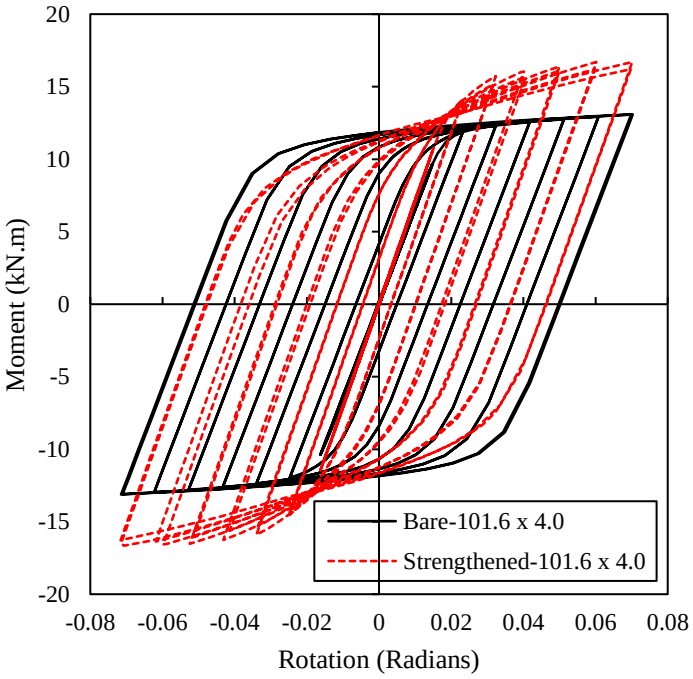

(c)

Figure 7: Moment-rotation hysteresis responses of the bare and strengthened CHS specimens with CFRP for (a) 101.6×3.2 and (b) 101.6×3.6 and (c) 101.6×4.0.

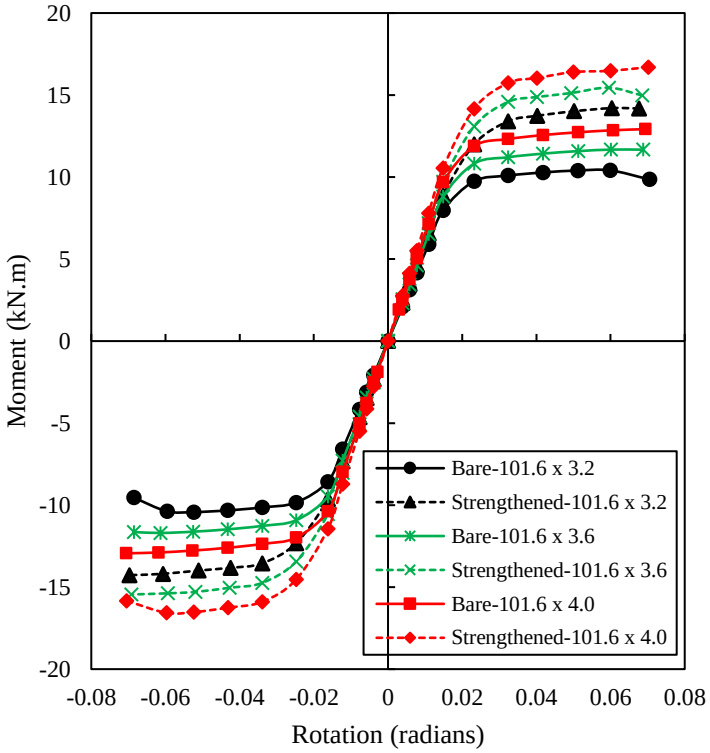
Moment (kN.m)
Rotation (radians)
Bare-101.6 x 3.2
Strengthened-101.6 x 3.2
Bare-101.6 x 3.6
Strengthened-101.6 x 3.6
Bare-101.6 x 4.0
Strengthened-101.6 x 4.0

(a)

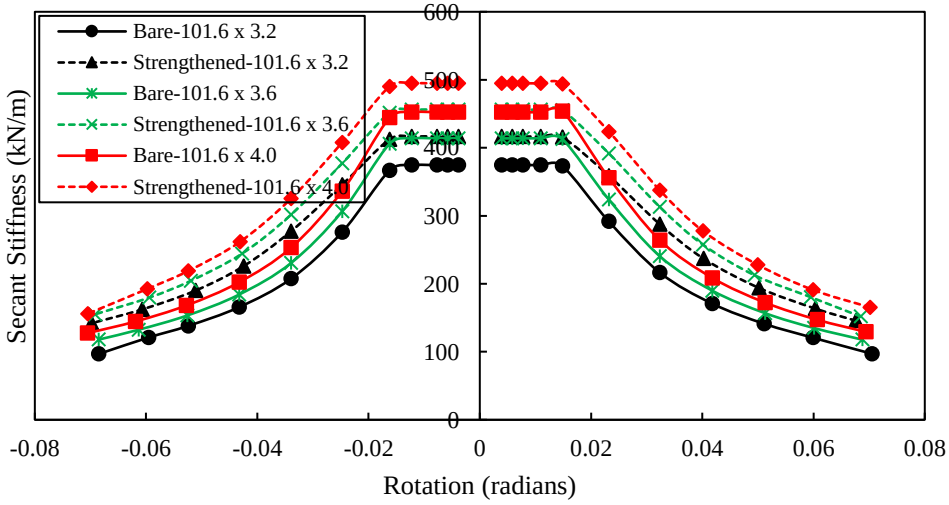
Secant Stiffness (kN/m)
Rotation (radians)
Bare-101.6 x 3.2
Strengthened-101.6 x 3.2
Bare-101.6 x 3.6
Strengthened-101.6 x 3.6
Bare-101.6 x 4.0
Strengthened-101.6 x 4.0

(b)

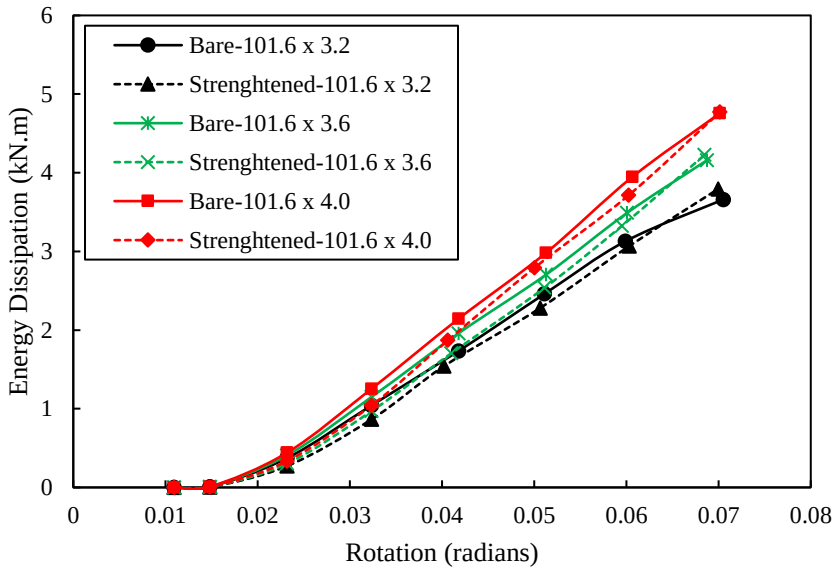

(c)

Figure 8: (a) Moment-rotation backbone responses (b) stiffness and (c) dissipation of energy of bare and CFRP strengthened CHS specimens with various t_{CFRP}/t_{CHS} ratios.

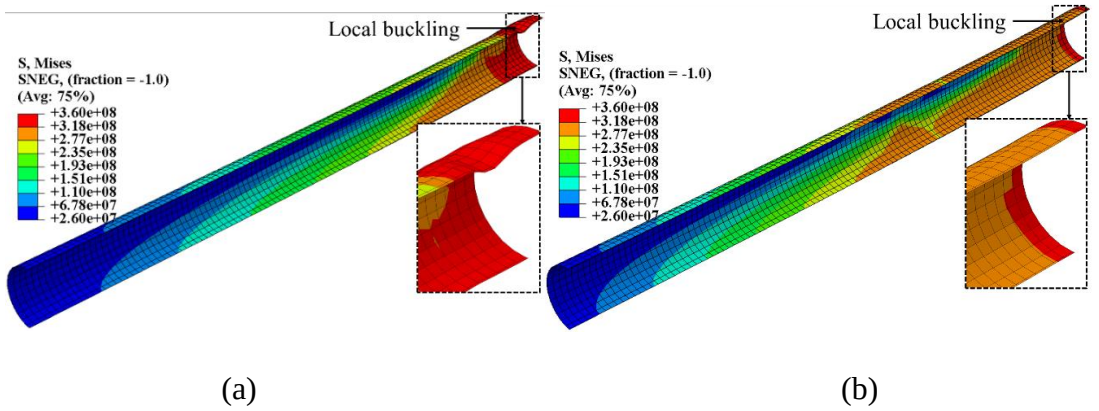

(a) (b)

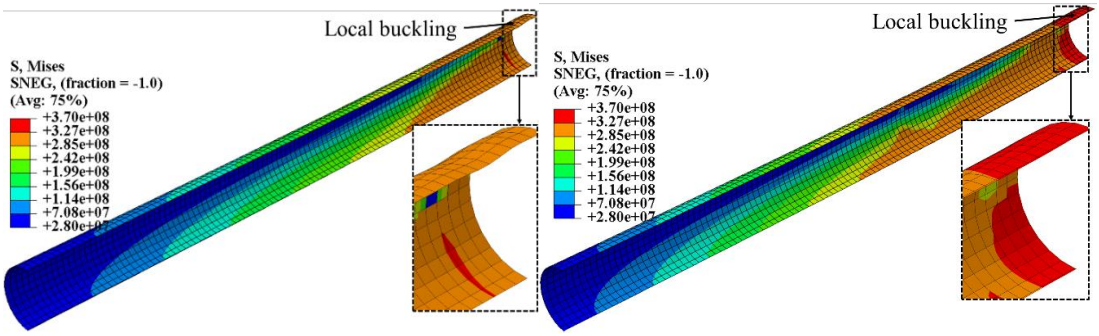

(c) (d)

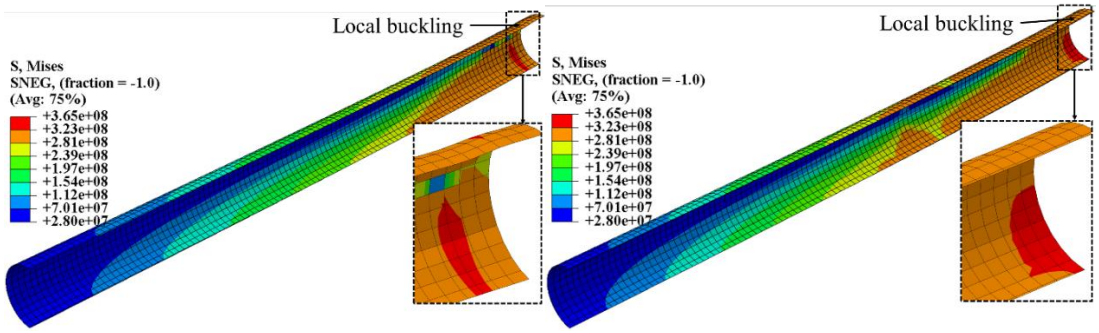

(e) (f)

Figure 9: Failure mode of steel section of (a) bare and (b) CFRP strengthened 101.6 ×3.2 CHS specimens, (c) bare and (d) CFRP strengthened 101.6 ×3.6 CHS specimens, (e) bare and (f) CFRP strengthened 101.6 ×4.0 CHS specimens.

4.4. Effect of the diameter-to-thickness ratio of CHS

In addition to the previous bare and CFRP strengthened CHS 101.6×4.0, two more bare and CFRP strengthened CHSs 139.7×4.0 and 193.7×4.0 are modelled and analysed under cyclic loading to predict the effect of the diameter-to-thickness ratio of CHS. Hence, the diameter-to-thickness ratio of CHS is increasing with the increasing of CHS outer diameter from 101.6 mm to 139.7 mm to 193.7 mm as the wall thickness of CHS remains constant. Results for the response parameters of moment capacity backbone response, ultimate moment capacity, stiffness and dissipation of energy are shown in Figure 10. It is interesting to note that the enhancements in the different structural response parameters under cyclic loading due to CFRP strengthening technique are not the same, although the properties of the material and the wrapping technique were the same. The improvements in the maximum moment capacities are 29.08%, 32.67% and 36.27% for CHSs with outer diameters of 101.6 mm, 139.7 mm and 193.7 mm respectively. Hence, the efficiency of CFRP strengthening increases with the increase of the diameter-to-thickness ratio of CHS under cyclic loading can be confirmed in the present study. A previous study [28] also concluded that the efficiency of CFRP strengthening

increases with the decrease in the compactness of the CHS specimens i.e. with the increase of the diameter-to-thickness ratio of CHS under four-point loading. The previous section showed that the efficiency of CFRP strengthening also increases with a decrease in the wall thickness of the CHS specimens. Both an increase in the diameter-to-thickness ratio and a decrease in the wall thickness result in a decrease of the CHS specimen's compactness. Moreover, the efficiency of CFRP strengthening to distribute the stresses more uniformly and to delay the local buckling of the CHS specimens can again be demonstrated from failure modes shown in Figure 11. The results from the present study show that cyclic performance increment of a CHS section due to CFRP strengthening is specimen specific and it is not possible to predict the cyclic performance increments of other CHS specimens due to CFRP strengthening with various t_{CFRP}/t_{CHS} ratio and/or diameter-to-thickness ratio of CHS. In this respect, the numerical modelling techniques developed and presented in this paper will be beneficial.

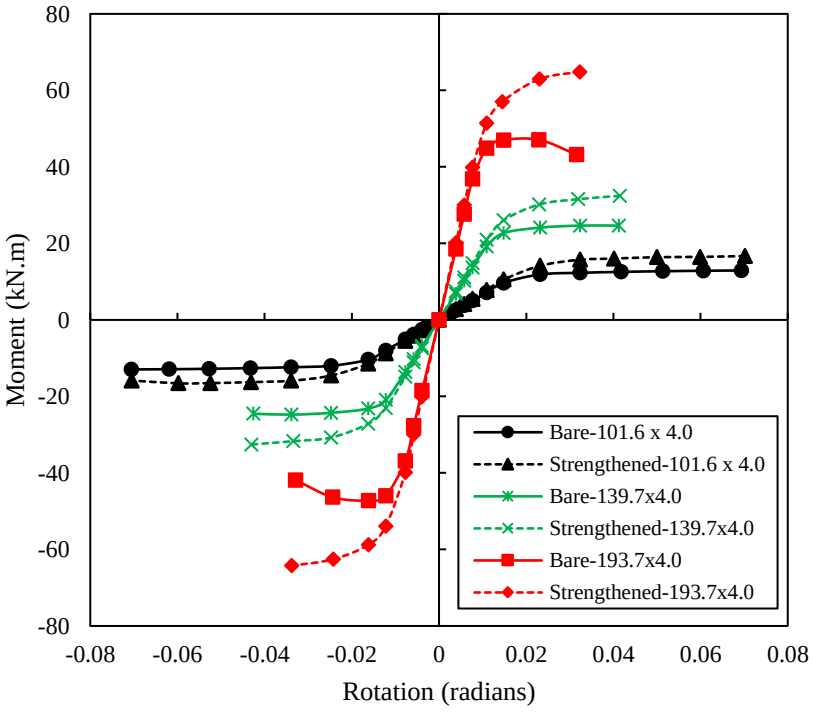

(a)

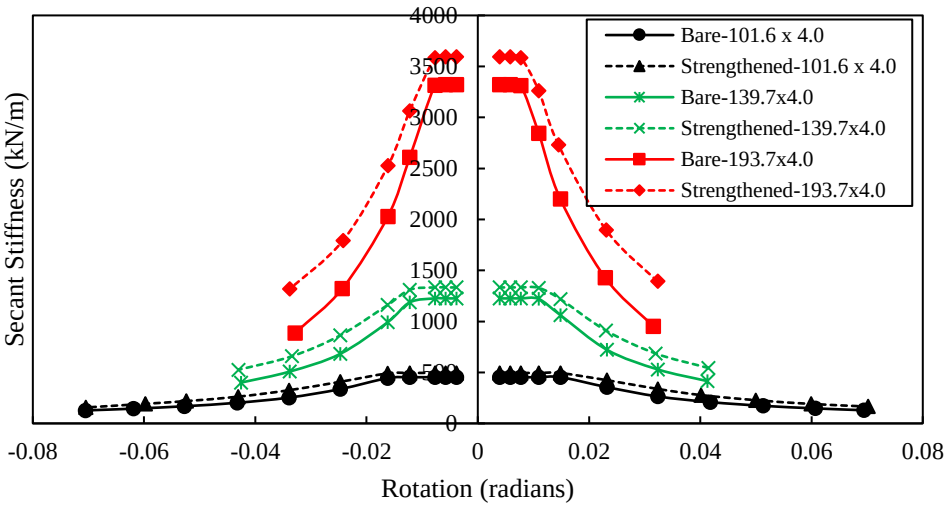

(b)

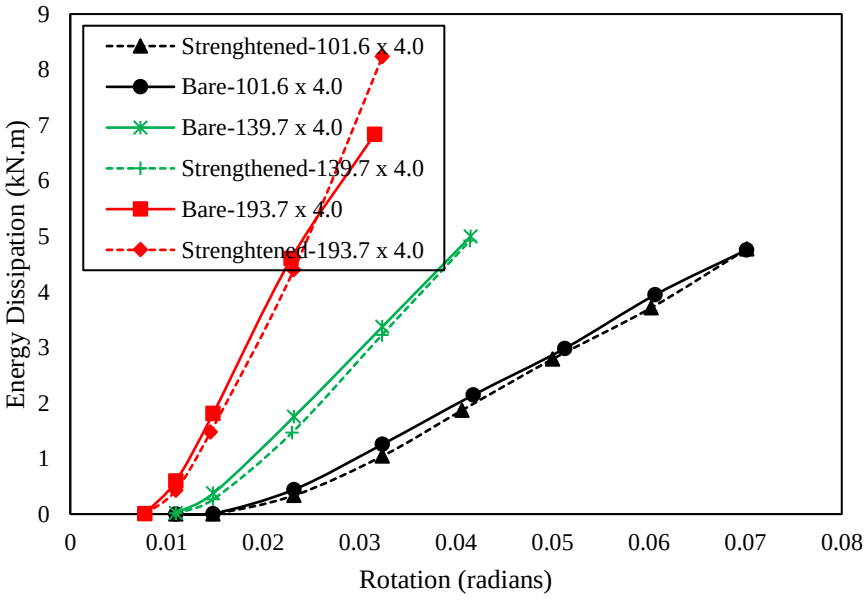

(c)

Figure 10: (a) Moment-rotation backbone responses (b) stiffness and (c) dissipation of energy of bare and CFRP strengthened CHS specimens with various diameter-to-thickness ratios.

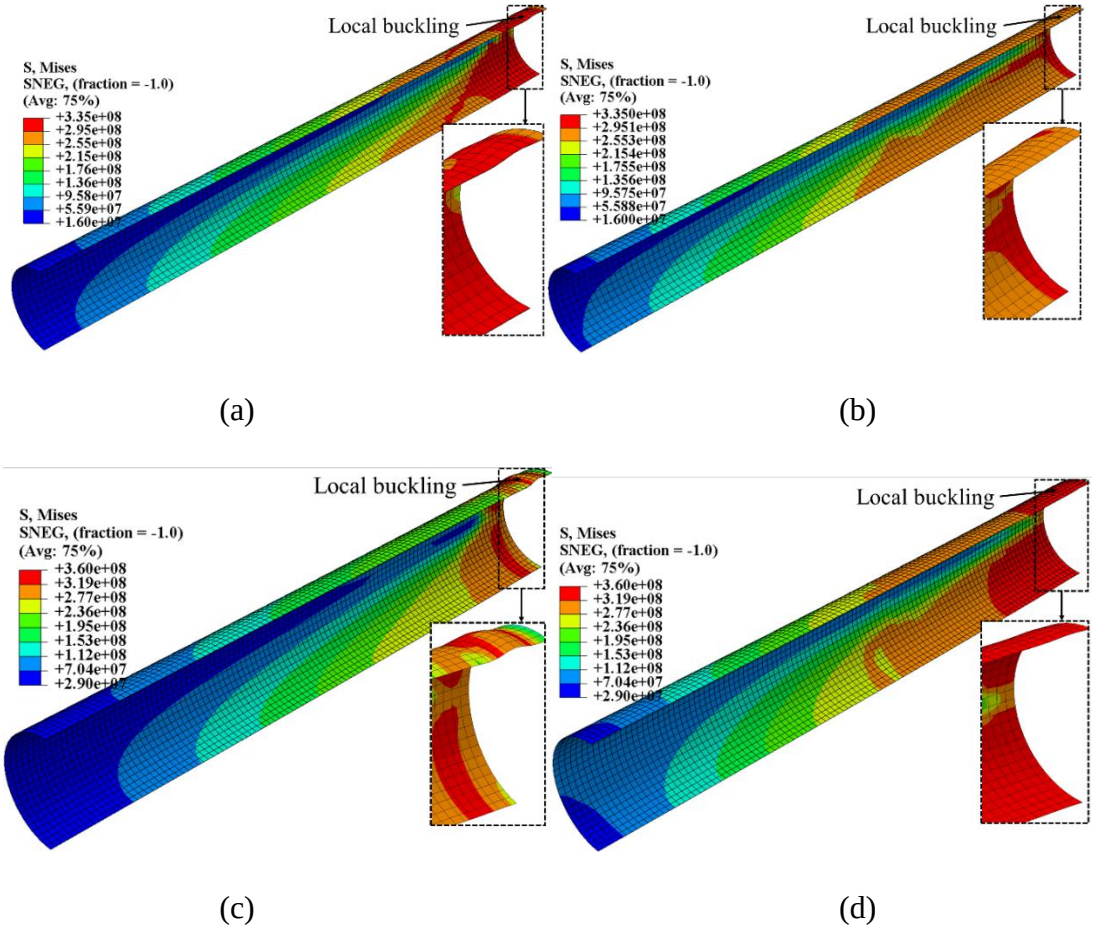

Figure 11: Failure mode of steel section of (a) bare and (b) CFRP strengthened 139.7×4.0 CHS specimens (c) bare and (d) CFRP strengthened 193.7×4.0 CHS specimens.

4.5. Effect of steel grade

The grade of steel is one of the important parameters of steel and today, higher grades of steel are commonly used. Three different steel grades of 250GPa, 350GPa and 450GPa are considered to investigate the effect of steel grade in the CFRP strengthening of CHS members under the cyclic loading. The structural response parameters of moment capacity backbone response, ultimate moment capacity, stiffness and dissipation of energy of the bare and CFRP strengthened CHS 101.6×4.0 specimens with various steel grades are compared in Figure 12. From the results, the efficiency of CFRP strengthening can be confirmed for all grades of steel and the improvements in the maximum moment capacities are 33.38%, 25.34% and 21.20%

for CHSs with steel grades of 250GPa, 350GPa and 450GPa respectively. Hence, the efficiency of CFRP strengthening reduces due to the increment of the steel grade.

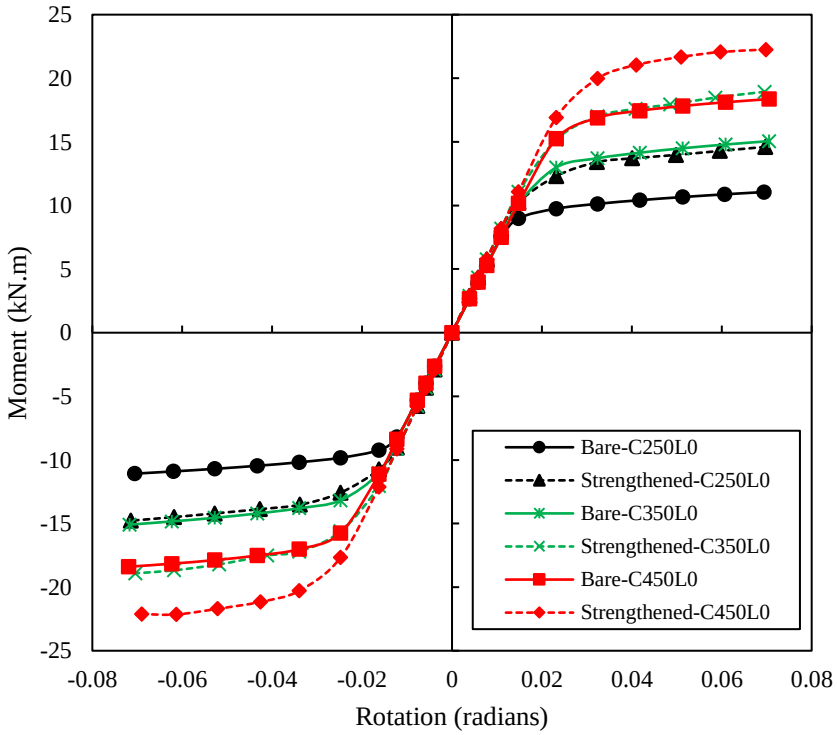

(a)

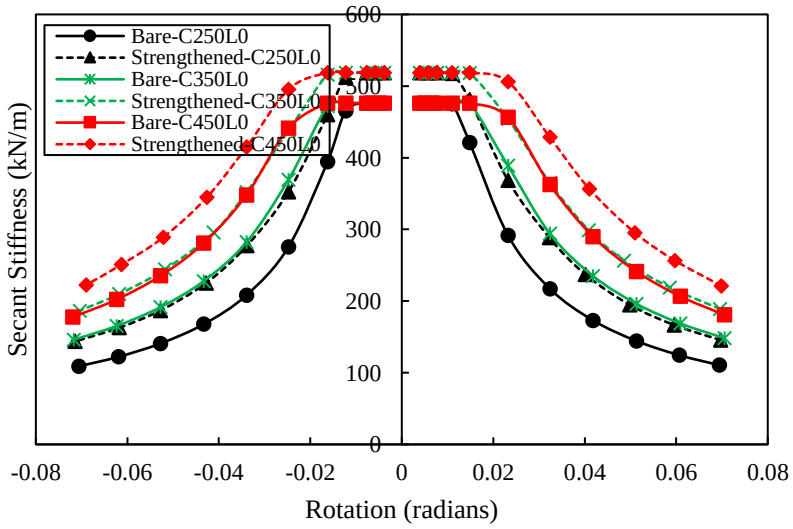

(b)

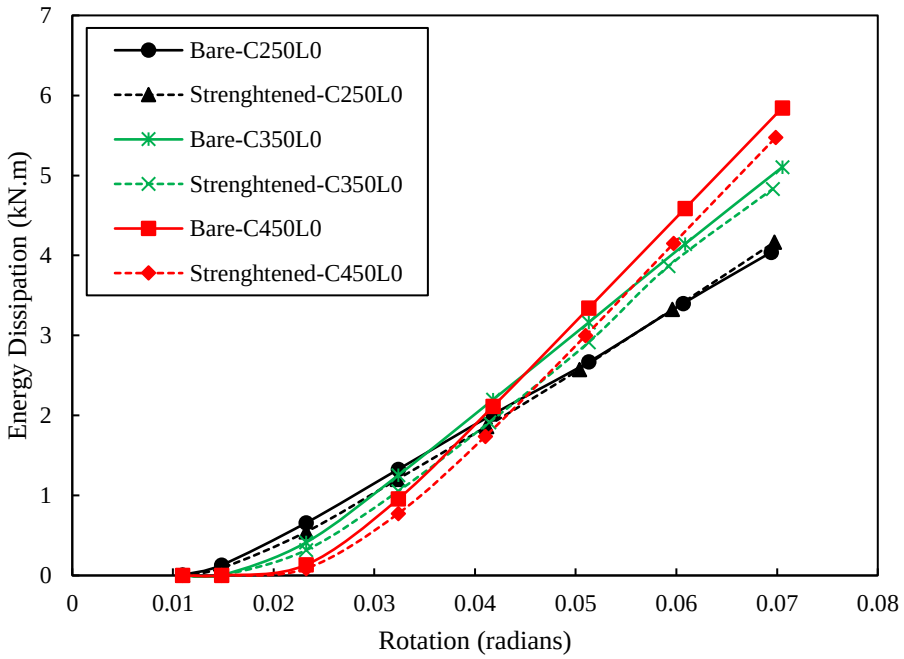

(c)

Figure 12: (a) Moment-rotation backbone responses (b) stiffness and (c) dissipation of energy of bare and CFRP strengthened CHS specimens with various steel grades.

5. Comparison of FE results with theoretically obtained results

The FE model simulated ultimate moment capacities of various bare and CFRP strengthened CHS specimens are compared with the theoretically obtained ultimate moment capacities based on the existing design model by Haedir et al. [28] by assuming some strain hardening. In the prediction model, the percentage of the strength of fibre effectiveness relative to steel (α_m) is chosen as 0.5 [45]. The transformed CFRP strengthened CHS section according to [28] to calculate the CFRP strengthened CHS beam moment capacity, is shown in Figure 13.

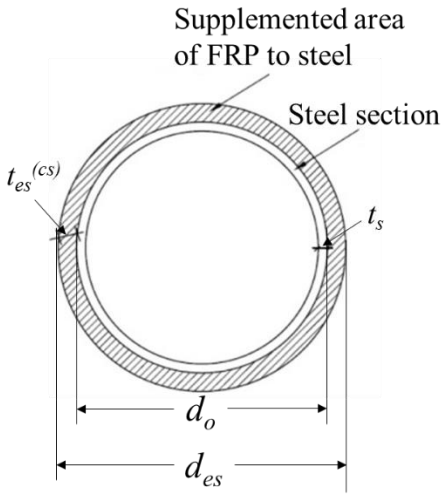

Figure 13:Transformed CFRP strengthened CHS section.

The diameter of the transformed section can be defined as below [28]:

$$d_{es} = d_o + 2\,t_{es}^{(cs)} \qquad \text{Equation 7}$$

where d_o is the outer diameter of the circular steel profile and $t_{es}^{(cs)}$ is the thickness of the supplanted area from CFRP to steel and specified by [28].

According to AS4100 (2016), section slenderness (λ_s) for a CHS shall be calculated as follows:

$$\lambda_s = \left(\frac{d_o}{t}\right)\left(\frac{f_y}{250}\right) \qquad \text{Equation 8}$$

The section slenderness (λ_s) for a CFRP strengthened CHS has rewritten as below [28]:

$$\lambda_{es} = \left(\frac{d_{es}}{t_{es}}\right)\left(\frac{f_y}{250}\right) \qquad \text{Equation 9}$$

in which d_{es} is expressed as in Equation 7 and t_{es} is the total thickness of the steel and the supplemented section given as $t_{es} = t_s + t_{es}^{(cs)}$.

The nominal section moment capacity of CFRP strengthened CHS beams (M_{es}) can be expressed as follows [28]:

$$M_{es} = f_y Z_{ese} \quad \text{Equation 10}$$

In the above equation, Z_{ese} refers to the effective section modulus of the equivalent steel section and it depends on the section classification, i.e. compact section, non-compact section or slender section and specified by Haedir et al. [28].

The theoretically obtained ultimate moment capacities based on an existing design model [28] have been multiplied by a cyclic design factor to consider the effect of quasi-static cyclic loading on the ultimate moment capacity of the section and assumed as 0.98, which is equal to the ratio between the experimental ultimate moment capacity under cyclic and monotonic loading [29]. Table 5 presents the comparison between the FE model simulated and theoretically obtained the ultimate moment capacities of various bare and CFRP strengthened CHS specimens. The FE model simulated moment capacities of various bare and CFRP strengthened CHS specimens closely match the theoretical predictions with a COV of 0.047 and a mean ratio of 0.98.

Table 5: Comparison of FE model simulated and theoretical ultimate moment capacities.

CHS member ID	Ultimate Moment capacity (kN.m)		$\frac{M_{FE}}{M_{Theo}}$
	Theoretical (M_{Theo})	FE analysis (M_{FE})	
101.6×4.0-Bare	12.86	12.94	1.01
101.6×4.0-Strengthened	17.95	16.70	0.93
101.6×3.6-Bare	11.67	11.70	1.00
101.6×3.6- Strengthened	16.76	15.45	0.92
101.6×3.2-Bare	10.46	10.43	1.00
101.6×3.2- Strengthened	15.54	14.27	0.92
139.7×4.0-Bare	24.85	24.75	1.00
139.7×4.0-Strengthened	34.40	32.84	0.95
193.7×4.0-Bare	46.64	47.24	1.01
193.7×4.0-Strengthened	66.81	64.37	0.96
C250L0-Bare	10.67	11.08	1.04
C250L0- Strengthened	14.89	14.78	0.99
C350L0-Bare	14.60	15.09	1.03
C350L0- Strengthened	20.38	18.91	0.93
C450L0-Bare	17.78	18.36	1.03
C450L0- Strengthened	24.82	22.26	0.90
		Mean	0.98
		COV	0.047

6. Conclusions

A numerical investigation on the cyclic performance of CFRP strengthened CHS specimens has been carried out in the present study. The FE modelling techniques were validated by comparing the simulated results with the authors' previously published experimental results [29]. The validated modelling techniques were then used to carry out a comprehensive parametric investigation on the effects of essential parameters such as the CFRP bond length, CFRP layer numbers, ratio of the thickness of CFRP composites (t_{CFRP}) to the wall thickness of CHS (t_{CHS}), CHS member diameter-to-thickness ratio and steel grade on the cyclic performance of CFRP strengthened CHS steel specimens. The structural performance parameters were moment capacity, energy dissipation capability and secant stiffness. Based on the results, the following conclusions can be drawn:

- The proposed FE modelling techniques can accurately predict the structural behaviour of different sized bare and CFRP strengthened CHS specimens under cyclic loading and this would enable saving the expenses and time of experimental investigations.
- For satisfactory enhancement of the different cyclic performance parameters, strengthening of the CHS steel specimens with three layers and 400 mm bond length of CFRP is recommended as the safest and most cost-effective way based on the specific span length and support condition considered in the present study. There is either insignificant or no change of the different cyclic responses of strengthened CHS steel specimens beyond strengthening with three layers and 400 mm bond length of CFRP.
- The efficiency of CFRP strengthening increases with an increase in the ratio of the thickness of CFRP to the thickness of CHS.
- The efficiency of CFRP strengthening increases with an increase in the diameter-to-thickness ratio of the CHS as the compactness of the CHS specimen decreases with an increase in its diameter-to-thickness ratio.

- CFRP strengthened CHS specimens showed less local buckling compared to the bare CHS specimens as the wrapped CFRP composites contribute to enhance the stiffness and distribute the stresses more uniformly.
- CFRP strengthening technique is effective for all grades of steel. The efficiency of CFRP strengthening reduces with an increase in the steel grade.
- The FE model simulated ultimate moment capacities show a reasonable agreement with the theoretically predicted values.

Acknowledgment

The authors wish to gratefully acknowledge the access to numerical software and high-performance computing (HPC) facilities provided by the Queensland University of Technology (QUT) to carry out the research reported in this study.

Data Availability Statement

At this time the processed/raw data required to regenerate the outcomes of the present study cannot be shared as these data are also a part of ongoing research.

References

[1] Wardenier J, Packer JA, Zhao XL, Van der Vegte GJ. Hollow sections in structural applications. Bouwen met Staal Rotterdam,, The Netherlands; 2002.

[2] Guha-Sapir D, Below R, Hoyois P. EM-DAT: International disaster database. Cathol Univ Louvain Brussels, Belgium 2015.

[3] ANSI/AISC 341-16. Seismic Provisions for Structural Steel Buildings, 2016. doi:111.

[4] Seica M V., Packer JA. FRP materials for the rehabilitation of tubular steel structures, for underwater applications. Compos Struct 2007;80:440–50. doi:10.1016/j.compstruct.2006.05.029.

[5] Kabir MH, Fawzia S, Chan THT, Badawi M. Numerical studies on CFRP strengthened steel circular members under marine environment. Mater Struct 2016;49:4201–16.

doi:10.1617/s11527-015-0781-5.

[6] Kabir MH, Fawzia S, Chan THT, Gamage JCPH. Comparative durability study of CFRP strengthened tubular steel members under cold weather. Mater Struct 2016;49:1761–74. doi:10.1617/s11527-015-0610-x.

[7] Saljoughian A, Mostofinejad D, Hosseini SM. CFRP confinement in retrofitted RC columns via CSB technique under reversed lateral cyclic loading. Mater Struct Constr 2019;52:1–14. doi:10.1617/s11527-019-1373-6.

[8] Triantafillou TC, Choutopoulou E, Fotaki E, Skorda M, Stathopoulou M, Karlos K. FRP confinement of wall-like reinforced concrete columns. Mater Struct Constr 2016;49:651–64. doi:10.1617/s11527-015-0526-5.

[9] Batuwitage C, Fawzia S, Thambiratnam D, Al-Mahaidi R. Durability of CFRP strengthened steel plate double-strap joints in accelerated corrosion environments. Compos Struct 2017;160:1287–98. doi:10.1016/j.compstruct.2016.10.101.

[10] Fawzia S, Al-Mahaidi R, Zhao XL, Rizkalla S. Strengthening of circular hollow steel tubular sections using high modulus CFRP sheets. Constr Build Mater 2007;21:839–45.

[11] Hollaway LC, Teng JG. Strengthening and Rehabilitation of Civil Infrastructures Using Fibre-Reinforced Polymer (FRP) Composites. Cambridge, U.K: Woodhead Publishing, Sawston, Cambridge, UK; 2008.

[12] Liu Y, Tafsirojjaman T, Dogar AUR, Hückler A. Shrinkage behavior enhancement of infra-lightweight concrete through FRP grid reinforcement and development of their shrinkage prediction models. Constr Build Mater 2020;258.

[13] Teng JG, Chen JF, Smith ST, Lam L. Behaviour and strength of FRP-strengthened RC structures: a state-of-the-art review. Proc Inst Civ Eng - Struct Build 2003;156:51–62. doi:10.1680/stbu.2003.156.1.51.

[14] Zhao XL, Zhang L. State-of-the-art review on FRP strengthened steel structures. Eng

Struct 2007;29:1808–23. doi:10.1016/j.engstruct.2006.10.006.

[15] Kabir MH, Fawzia S, Chan THT, Gamage JCPH, Bai JB. Experimental and numerical investigation of the behaviour of CFRP strengthened CHS beams subjected to bending. Eng Struct 2016;113:160–73. doi:10.1016/j.engstruct.2016.01.047.

[16] Alam MI, Fawzia S. Numerical studies on CFRP strengthened steel columns under transverse impact. Compos Struct 2015;120:428–41. doi:10.1016/j.compstruct.2014.10.022.

[17] Tafsirojjaman T, Fawzia S, Thambiratnam D, Zhao XL. Seismic strengthening of rigid steel frame with CFRP. Arch Civ Mech Eng 2019;19:334–47. doi:10.1016/j.acme.2018.08.007.

[18] Tafsirojjaman, Fawzia S, Thambiratnam D. Enhancement Of Seismic Performance Of Steel Frame Through CFRP Strengthening. Procedia Manuf 2019;30:239–46. doi:10.1016/j.promfg.2019.02.035.

[19] Tafsirojjaman T, Fawzia S, Thambiratnam D. Numerical investigation on the CFRP strengthened steel frame under earthquake. Mater. Sci. Forum Front. Compos. Mater. IV, Trans Tech Publications Ltd.; 2019.

[20] Tafsirojjaman T, Fawzia S, Thambiratnam D. Numerical investigation on the seismic strengthening of steel frame by using normal and high modulus CFRP. Proc. seventh Asia-Pacific Conf. FRP Struct., International Institute for FRP in Construction (IIFC); 2019.

[21] Alam MI, Fawzia S, Tafsirojjaman T, Zhao XL. FE modeling of FRP strengthened CHS members subjected to lateral impact. Tubul. Struct. XVI Proc. 16th Int. Symp. Tubul. Struct. (ISTS 2017, 4-6 December 2017, Melbourne, Aust., CRC Press; 2017, p. 409.

[22] Harries KA, Peck AJ, Abraham EJ. Enhancing stability of structural steel sections using FRP. Thin-Walled Struct 2009;47:1092–101. doi:10.1016/j.tws.2008.10.007.

[23] Fernando ND. Bond behaviour and debonding failures in CFRP-strengthened steel members. The Hong Kong Polytechnic University, 2010.

[24] Xiao Z-G, Zhao X-L. CFRP repaired welded thin-walled cross-beam connections subject to in-plane fatigue loading. Int J Struct Stab Dyn 2012;12:195–211.

[25] Chen T, Qian-Qian Y, Xiang-lin G. Study on fatigue behavior of strengthened non-load-carrying cruciform welded joints using carbon fiber sheets 2012;12:179–94. doi:10.1142/S0219455412004586.

[26] Nakamura H, Jiang W, Suzuki H, Maeda, Irube T. Experimental study on repair of fatigue cracks at welded web gusset joint using CFRP strips. Thin-Walled Struct 2009;47:1059–68. doi:10.1016/j.tws.2008.10.016.

[27] Gholami M, Sam ARM, Yatim JM, Tahir MM. A review on steel/CFRP strengthening systems focusing environmental performance. Constr Build Mater 2013;47:301–10. doi:10.1016/j.conbuildmat.2013.04.049.

[28] Haedir J, Bambach MR, Zhao XL, Grzebieta RH. Strength of circular hollow sections (CHS) tubular beams externally reinforced by carbon FRP sheets in pure bending. Thin-Walled Struct 2009;47:1136–47. doi:10.1016/j.tws.2008.10.017.

[29] Tafsirojjaman T, Fawzia S, Thambiratnam D, Zhao XL. Behaviour of CFRP strengthened CHS members under monotonic and cyclic loading. Compos Struct 2019;220:592–601. doi:10.1016/j.compstruct.2019.04.029.

[30] Photiou N, Hollaway LC, Chryssanthopoulos MK. Strengthening Of An Artificially Degraded Steel Beam Utilising A Carbon/Glass Composite System. Adv Polym Compos Struct Appl Constr ACIC 2004 2004;20:274–83. doi:10.1016/B978-1-85573-736-5.50030-3.

[31] Simulia DS. ABAQUS/CAE 6.21. ABAQUS Anal Theory Manuals, SIMULIA, Dassault Systèmes, Realis Simulation, Provid RI, USA 2020.

[32] Tafsirojjaman T, Fawzia S, Thambiratnam D, Zhao X. Numerical investigation of CFRP strengthened RHS members under cyclic loading. Structures 2020;24:610–26. doi:10.1016/j.istruc.2020.01.041.

[33] Alam MI, Fawzia S, Liu X. Effect of bond length on the behaviour of CFRP strengthened concrete-filled steel tubes under transverse impact. Compos Struct 2015;132:898–914. doi:10.1016/j.compstruct.2015.06.065.

[34] Al-Zubaidy H, Al-Mahaidi R, Zhao XL. Finite element modelling of CFRP/steel double strap joints subjected to dynamic tensile loadings. Compos Struct 2013;99:48–61. doi:10.1016/j.compstruct.2012.12.003.

[35] Al-Mosawe A, Al-Mahaidi R, Zhao XL. Effect of CFRP properties, on the bond characteristics between steel and CFRP laminate under quasi-static loading. Constr Build Mater 2015;98:489–501. doi:10.1016/j.conbuildmat.2015.08.130.

[36] Teng JG, Fernando D, Yu T. Finite element modelling of debonding failures in steel beams flexurally strengthened with CFRP laminates. Eng Struct 2015;86:213–24. doi:10.1016/j.engstruct.2015.01.003.

[37] Nunes F, Correia JR, Silvestre N. Structural behavior of hybrid FRP pultruded beams: Experimental, numerical and analytical studies. Thin-Walled Struct 2016;106:201–17. doi:10.1016/j.tws.2016.05.004.

[38] Faggiani A, Falzon BG. Predicting low-velocity impact damage on a stiffened composite panel. Compos Part A Appl Sci Manuf 2010;41:737–49. doi:10.1016/j.compositesa.2010.02.005.

[39] Naghipour P, Schneider J, Bartsch M, Hausmann J, Voggenreiter H. Fracture simulation of CFRP laminates in mixed mode bending. Eng Fract Mech 2009;76:2821–33. doi:10.1016/j.engfracmech.2009.05.009.

[40] Benzeggagh ML, Kenane M. Measurement of mixed-mode delamination fracture

toughness of unidirectional glass/epoxy composites with mixed-mode bending apparatus. Compos Sci Technol 1996;56:439–49.

[41] Hashin Z. Failure criteria for unidirectional fibre composites. ASME J Appl Mech 1980;47:329–34.

[42] Hashin Z, Rotem A. A Fatigue Failure Criterion for Fiber Reinforced Materials. J Compos Mater 1973;7:448–64. doi:10.1177/002199837300700404.

[43] Lesani M, Bahaari MR, Shokrieh MM. Numerical investigation of FRP-strengthened tubular T-joints under axial compressive loads. Constr Build Mater 2014;53:243–52. doi:10.1016/j.conbuildmat.2013.11.097.

[44] Imran M, Mahendran M, Keerthan P. Experimental and numerical investigations of CFRP strengthened short SHS steel columns. Eng Struct 2018;175:879–94. doi:10.1016/j.engstruct.2018.08.042.

[45] Kabir MH, Fawzia S, Chan THT, Gamage JCPH. Durability performance of carbon fibre-reinforced polymer strengthened circular hollow steel members under cold weather. Aust J Struct Eng 2014;15:377–92. doi:10.7158/S13-042.2014.15.4.

[46] AS 4100: Steel structures, Standards Australia. 2016.